Mechanical Systems and Signal Processing 204 (2023) 110760

Contents lists available at ScienceDirect

Mechanical Systems and Signal Processing

journal homepage: www.elsevier.com/locate/ymssp

Data-driven modeling and analysis of nonlinear isolated mechanical system

Sunit Kumar Gupta [a], Mohammad A. Bukhari [b], Oumar R. Barry [a,*], Chinedum Okwudire [c]

[a] Department of Mechanical Engineering, Virginia Tech Blacksburg, Virginia 24061, USA,
[b] Department of Mechanical Engineering, Wayne State University, Detroit, Michigan 48202, USA,
[c] Department of Mechanical Engineering, University of Michigan, Ann Arbor, Michigan 48109, USA

ARTICLE INFO

Communicated by S. Laflamme

Keywords:
System identification
Stability analysis
Data-driven modeling
Bifurcation analysis

ABSTRACT

This study aims to identify nonlinearities in the stiffness and damping characteristics of a passive pneumatic isolator connected to an ultra-precision manufacturing prototype in the uncoupled transverse and horizontal directions. Experimental data are collected using sine sweep tests and is used to plot nonlinear frequency response functions. The resulting analysis reveals a quadratic polynomial relationship between the equivalent stiffness and the system's dynamic response, indicating a combination of quadratic and cubic nonlinearity. Similarly, the nonlinear damping characteristic is determined using the half-power bandwidth method, which exhibits a quadratic polynomial relationship between the equivalent damping and dynamic response. The linear stability analysis of the system for the identified nonlinear stiffness and damping characteristics reveals that the system remains linearly stable for the given range of frequency and excitation amplitudes. Furthermore, bifurcation analysis reveals the existence of complex solutions, such as period-2 and period-4 solutions, for higher excitation amplitudes.

1. Introduction

The dependence of the manufacturing industry on ultra-precision manufacturing (UPM) machines has increased over the past few decades [1–3]. UPM machines, such as ultra-precision machine tools, wafer scanners, and micro-coordinate measurement machines, are in high demand due to their use in applications like telecommunications, defense, and biomedical products [4–7]. However, the high complexity and surface finish requirements (1–100 nm) of these components make UPM machines highly susceptible to small-amplitude disturbances from the ground or surroundings, which can significantly impact their accuracy and performance [8].

One of the strategies to control these unwanted vibrations is the effective isolation of UPM through either passive, active, or semi-active isolators [9–12]. Passive isolators in the form of pneumatic isolators are often preferred over semi-active or active isolators for UPM machines due to their simple design, cost-effectiveness, reliability, energy efficiency, and ease of installation [8,10,13]. Moreover, the popularity of pneumatic isolators in UPM machines [10,14,15] can be attributed to two major factors; (1) pneumatic isolators support high payloads using relatively low energy, and (2) they exhibit low transmissibility at frequencies higher than the resonance frequencies in contrary to viscously damped isolators [16,17]. Also, they are effective at attenuating vibrations over a wide range of frequencies, especially when the excitation frequencies are sufficiently above the natural frequencies of the system (2–6 Hz) [10,18–20]. Accordingly, pneumatic isolators have been a frequent topic of study, especially concerning the dynamic behavior

* Corresponding author.
E-mail address: obarry@vt.edu (O.R. Barry).

https://doi.org/10.1016/j.ymssp.2023.110760
Received 11 May 2023; Received in revised form 19 July 2023; Accepted 5 September 2023
Available online 13 September 2023
0888-3270/Published by Elsevier Ltd.

associated with these isolators. A linear dynamical model of a pneumatic isolator for UPM machines can be easily obtained [3] and is valid for small payload displacement, (i.e., less than 5 μm). However, for larger payload displacements, a linear model is insufficient to predict the dynamics accurately, necessitating the use of a nonlinear model of the pneumatic isolator. The nonlinearity in the pneumatic isolator can arise from different factors such as the diaphragm, flow restrictor, and compressibility of air in the chambers. Therefore, to accurately predict the dynamic behavior of pneumatic-isolated UPM machines, it is necessary to establish nonlinear characteristics of pneumatic isolators. In this work, we aim to highlight the effect of nonlinearity in pneumatic isolators using experimental data and existing system identification methods.

Analytical models for the stiffness and damping characteristics of the pneumatic isolator have been extensively studied in the literature, relying on the thermodynamic properties of air and modeling the diaphragm as pneumatic springs [21–25]. These models were further verified through experiments. However, these models do not explicitly describe the dependence of the stiffness and damping characteristics on the states of the system (position and velocity). Therefore, it becomes challenging to conduct a nonlinear analytical study to establish the nature of bifurcation and the existence of different nonlinear attractors in the system using these analytical models of pneumatic isolators. While some studies, such as Heertjes and Wouw [26] have provided an explicit dependence of nonlinear stiffness on displacement, they lack experimental verification. Therefore, for the first time, this work aims to develop the closed-forms for the explicit nonlinear stiffness and damping characteristics through experiments on a pneumatic isolator supporting the reconfigurable prototype of UPM.

To determine the dynamic characteristics of a system, it is necessary to perform forced or free vibration tests and update the system's mathematical model. This further clarifies the influence of different parameters on the system dynamics. Frequency domain methods are advantageous for identifying the nonlinear characteristics of the system as obtaining the frequency response function using the sine sweep test is relatively easy [27–30], relatively robust to the noise in the signal, independent of the prior knowledge of the model and straightforward in comparison to other methods to identify nonlinear characteristics of the system [31–34]. In this study, we follow a method proposed by Liu et al. [30] to identify the nonlinear restoring force in the system. This method exploits the concept that nonlinear structures exhibit linear behavior under the steady-state response, allowing the equivalent stiffness of the system to be obtained for different excitation amplitudes [27–31]. The nonlinear stiffness of the system is then obtained through curve fitting using the harmonic balance method. The proposed method [30] also evaluates the damping characteristics of the system using the half-power bandwidth method and the frequency response function plot. Experimental results and corresponding empirical models reveal softening nonlinearity in the stiffness and damping characteristics of the pneumatic isolator as functions of displacements and velocity in the y- and z-directions. Furthermore, the linear stability analysis of the system reveals that for the identified nonlinear parameters, the system remains stable for a broader range of excitation amplitudes and is consistent with experimental results.

The rest of the paper is organized as follows. Section 2 presents the experimental setup, followed by the analytical model of system and parameter identification method in Section 3. Results and discussion are presented in Section 4 with the linear stability analysis in Section 5. Finally, some conclusions are drawn in Section 6.

2. Experimental setup

Experiments are conducted using a reconfigurable prototype of UPM. The experimental rig and schematic are depicted in Figs. 1 and 2, respectively. The prototype consists of an 800 kg base with the dimensions $749.3 \times 749.3 \times 495.3$ mm and is supported by four pneumatic isolators (Bilz model BiAir 1-ED) at the four corners. We emphasize that as the experimental setup exhibits symmetry in the x–y plane, we conduct experiments in one of these directions [2]. More specifically, we select y-direction to conduct the experiments. To estimate the stiffness and damping characteristic of the pneumatic isolator in the y- and z-directions, it is necessary to decouple all the modes viz. transverse, horizontal, and rocking motion. This step ensures that the dynamical characteristics of the pneumatic isolator in one direction do not influence the motion of the prototype in the other direction and eliminates any cross-coupling effects between the two directions. To achieve this decoupling, the prototype is reconfigured such that its center of gravity aligns with the location of the isolators. For more details readers are referred to [2,35].

For the experimental analysis, the prototype is excited using an inertial shaker (APS Dynamics model APS 113, frequency range DC..200 Hz) in the form of sine-sweep signals applied separately in the y- and z- directions. It is important to note that the inertial shaker is bolted securely to the structure for accurate excitation. This step further ensures that the nonlinearity of the shaker does not influence the modes of the UPM prototype. The digital signal processor (DSP) receives commands from the computer interface to generate the excitation signals, which are amplified by a power amplifier and then applied to the shaker. An accelerometer (PCB 393B05) is mounted on the shaker to measure the base excitation, while another accelerometer is installed on the prototype to measure the output response of the isolated system. Sine-sweep tests are conducted by varying the excitation levels to investigate the nonlinear behavior of the system.

3. Modeling and parameter identification method

This section presents the analytical model for the UPM prototype and the pneumatic isolators. Fig. 3 illustrates the front view of the experimental setup and the schematic of the analytical model. The UPM prototype's motion in the y- and z-directions is modeled using a two-degree-of-freedom system. The prototype, with mass m, can translate in both directions. The pneumatic isolators, positioned on both sides along the y-axis, are modeled as spring–damper systems (Fig. 3(ii)). Similarly, the isolators in the z-direction are modeled separately as spring-damper system. Therefore, the combined stiffness of the isolators in the y-direction

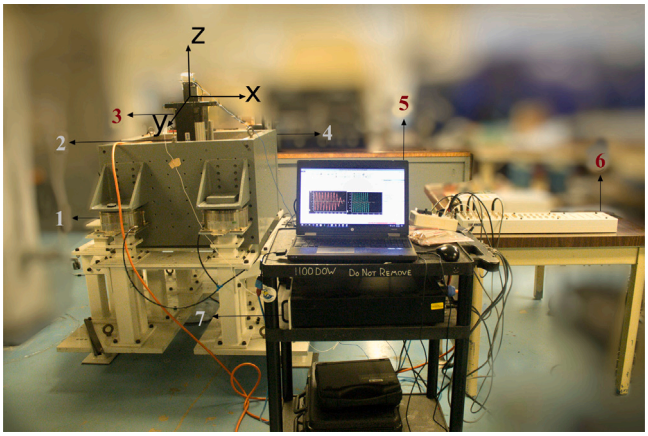

Fig. 1. Experimental rig: A reconfigurable UPM machine prototype with the following elements (1) Pneumatic isolators (Bilz model BiAir 1-ED), (2) shear accelerometer (PCB 393B05), (3) electromagnetic shaker (APS Dynamics model APS 113), (4) base, (5) Graphical user interface (GUI), (6) DSP, and (7) signal amplifier.

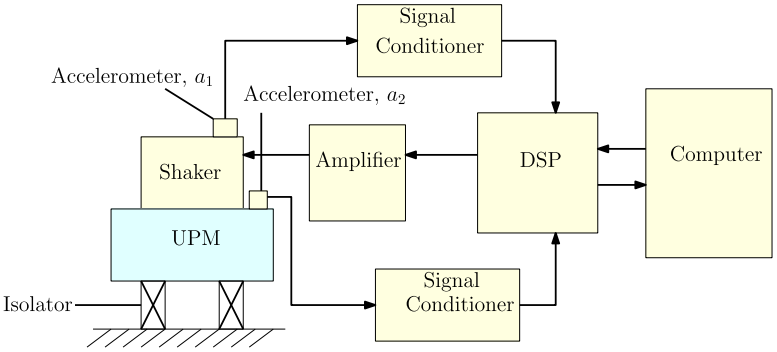

Fig. 2. Schematic of experimental rig.

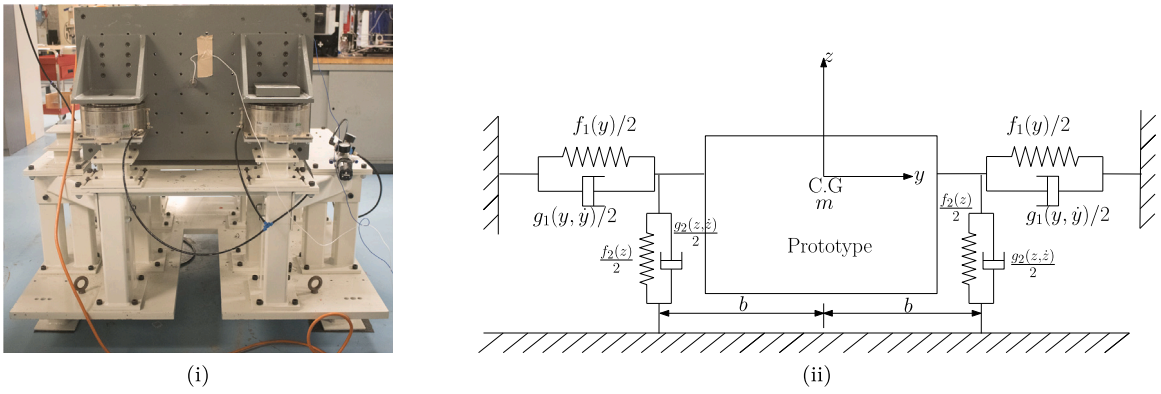

Fig. 3. (i) Front view of the experimental setup, and (ii) schematic of the experimental setup.

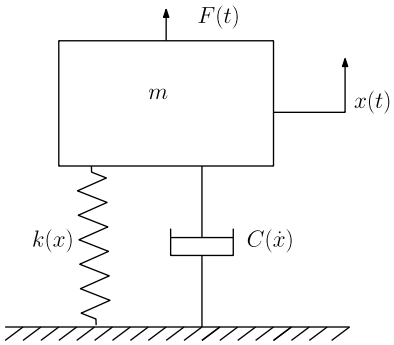

Fig. 4. Lumped spring–mass–damper system.

is represented by $f_1(y)$, while $f_2(z)$ represents the combined stiffness in the z-direction. Similarly, the combined damping of the pneumatic isolators in the y-direction is represented by $g_1(y, \dot{y})$, and $g_2(z, \dot{z})$ represents the combined damping in the z-direction. For simplicity in parameter identification, we assume that damping in both directions depends only on velocity.

As mentioned earlier in Section 2, the decoupling of the prototype's motion in the y and z-directions is achieved by aligning the center of gravity of the prototype with the isolator positions. Consequently, any perturbation in the y-direction (or z-direction) will result in motion in the y-direction (or z-direction) only. Thus, the governing equations of motion for the system in the y- and z-directions can be written as:

$$m\ddot{y} + f_1(y) + g_1(\dot{y}) = 0\,, \tag{1a}$$

$$m\ddot{z} + f_2(z) + g_2(\dot{z}) = 0\,. \tag{1b}$$

Furthermore, if the system is externally excited in the y-direction, the governing equation of motion becomes:

$$m\ddot{y} + f_1(y) + g_1(\dot{y}) = F_y\,, \tag{2}$$

where F_y is the external force in the y-direction. Similarly, if the system is externally excited in the z-direction, the governing equation of motion becomes

$$m\ddot{z} + f_2(z) + g_2(\dot{z}) = F_z\,, \tag{3}$$

where F_z is the external force in the z-direction.

Next, we outline the methods for evaluating the stiffness and damping functions of a pneumatic isolator. For this purpose, we consider a single-degree-of-freedom spring–mass–damper system, as shown in Fig. 4

The system is governed by the equation of motion

$$m\ddot{x} + C(\dot{x}) + k(x) = F(t)\,, \tag{4}$$

where m, x, and $F(t)$ are known quantities, while $C(\dot{x})$ and $k(x)$ are unknown. Liu et al. [30] proposed a method for identifying these unknown quantities using the frequency response surface function plot. The method is based on the principle that the vibration energy of the system is concentrated in the excitation frequency, allowing the vibration response to be approximated as linear during the steady-state response. Under harmonic excitation of amplitude F_0 and frequency ω, $F(t) = F_0 e^{i\omega t}$, the steady-state response of the system can be written as:

$$x(t) = X_0 e^{i(\omega t + \phi)}\,, \tag{5}$$

where X_0 is the response of the system and ϕ is the phase difference. Also, during the steady-state response, the system can be represented as

$$m\ddot{x} + C_{eq}\dot{x} + K_{eq}x = F(t)\,. \tag{6}$$

where K_{eq} and C_{eq} represent equivalent stiffness and damping, respectively. By utilizing Eqs. (4), (5), (6), and the harmonic balance method, the equivalent stiffness K_{eq} and damping C_{eq} can be given by

$$K_{eq} = \frac{1}{\pi X_0}\int_0^{2\pi} k(x)\sin(\boldsymbol{\Phi})\mathrm{d}\boldsymbol{\Phi}\,, \tag{7}$$

$$C_{eq} = \frac{1}{\pi\omega X_0}\int_0^{2\pi} C(\dot{x})\cos(\boldsymbol{\Phi})\mathrm{d}\boldsymbol{\Phi}\,. \tag{8}$$

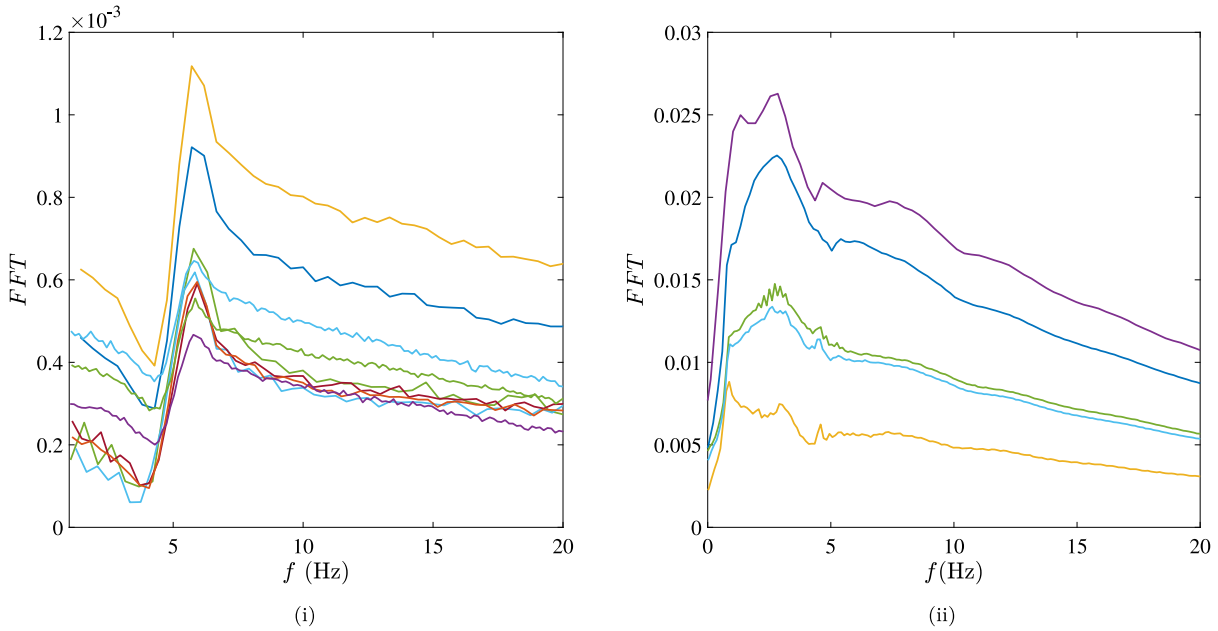

Fig. 5. FFT of output acceleration signal through impact test in the (i) y-direction, and (ii) z-direction for different impact values.

with $\Phi = \omega t + \phi$. Therefore, if K_{eq} and C_{eq} are known functions of the dynamic response, i.e., X_0; the nonlinear stiffness $k(x)$ and damping $C(\dot{x})$ can be estimated for the given system. It should be noted that although equivalent stiffness is a linear concept, the variation of equivalent linear stiffness or damping characteristics with different frequencies is a well-known method to estimate nonlinear stiffness and damping functions. This method utilizes the fact that a nonlinear system exhibits linear behavior under the steady-state response, and hence, the solution can be expressed in terms of harmonic functions. Expressing the steady-state response of a nonlinear system through a harmonic function or sum of harmonic functions is known as the harmonic balance method. This is a well-known method to determine the dynamics of a nonlinear system, which further ensures the preservation of system stability during curve fitting (Eqs. (7) and (8)). To determine $k(x)$ and $C(\dot{x})$, Liu et al. [30] utilized the nonlinear frequency response function (FRF) plots. The nonlinear FRF varies as the excitation amplitude increases, indicating either softening or hardening behavior. By plotting the nonlinear FRF from experimental data for different excitation amplitudes, the resonant frequencies ω_r can be extracted for different dynamic response values X_0. Once the resonant frequencies are known for different values of X_0, K_{eq} can be estimated for each dynamic response using the relationship between mass, frequency, and stiffness. Later, $K(X_0)$ is determined using a curve-fitting approach. To determine $C(X_0\omega)$, we can either implement the half-power bandwidth method, up to the first-order expansion of damping ratio [36,37], or use the circle-fit method [38]. However, the circle-fit method requires the estimation of amplitude as well as phase, while the half-power bandwidth only requires amplitude. Therefore, for the sake of simplicity in the analysis, we use the half-power bandwidth method. If ω_1 and ω_2 ($\omega_2 > \omega_1$) are the two frequencies at which the FRF amplitude is equal to $1/\sqrt{2}$ times the maximum amplitude of FRF at the resonance frequency ω_r, then the relationship between the damping ratio ζ, ω_1, ω_2, and ω_r is given by [36,37]

$$2\zeta = \frac{\omega_2 - \omega_1}{\omega_r}. \tag{9}$$

Using these values of ζ, along with mass and ω_r, C_{eq} can be estimated for different values of dynamic response X_0. Furthermore, similar to $k(X_0)$, $C(X_0\omega)$ can be obtained by curve-fitting between C_{eq} and X_0, which will provide us with the nonlinear damping function.

4. Experiments and parameter identification

In this section, we perform parameter identification of the pneumatic isolator considered in the analysis. The parameter identification task is divided into three sub-tasks: (1) identifying whether the system exhibits nonlinear characteristics in stiffness and damping properties, (2) determining the type of nonlinearity, and (3) establishing the parameter values that best describe the nonlinear behavior. To achieve this, we employ a combination of experimental and analytical approaches, specifically the harmonic balance method and the half-power bandwidth method. The first two sub-tasks can be accomplished using experimental results, while the final task of evaluating the parameters is achieved through the analytical model of equivalent stiffness and damping characteristics and the curve-fitting approach.

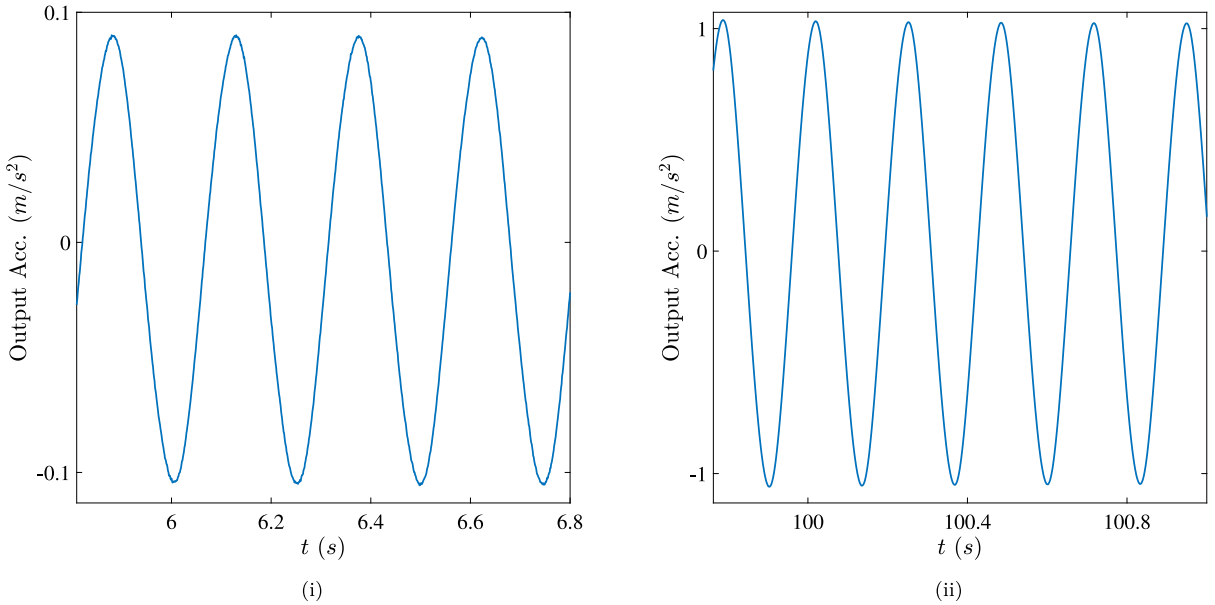

Fig. 6. Time response of the system in terms of output acceleration in y-direction for (i) in forward sweep, and (ii) in backward sweep.

To identify the parameters of the pneumatic isolator in the y and z directions, we perform two different sets of experiments using two different configurations. In one configuration, the shaker is securely fixed to the structure in such a manner that the armchair moves in the y direction, exciting the prototype in the y- direction only. In the other configuration, the shaker is fixed to move the armchair in the z- direction, exciting the system in the z- direction only. To plot the FRF of the prototype at different excitation amplitudes, we conduct sine-sweep tests in the forward (increasing excitation frequency) and backward directions (decreasing excitation frequency) and collect input and output acceleration signals. We repeat these experiments three times for every excitation value to ensure results are reproducible. However, to determine the range of the sine-sweep test, we need to know the system's fundamental frequency. We obtain the system's fundamental frequency by performing modal impact testing on the prototype using a modal impact hammer with a hard tip in the y- and z- directions. The Fast Fourier Transform (FFT) of the output acceleration signal with frequency f is shown in Fig. 5, where we observe that the first resonant frequency of the system is around 5.5 Hz in the y- direction and around 3 Hz in the z- direction. We also observe that the system dynamics are dominated by the first mode in both directions.

After obtaining the first resonant frequencies in the y- and z- directions, we select the ranges of 4–7 Hz and 1.5–4 Hz for the sine-sweep tests in the y- and z- directions, respectively, with a frequency step size of 0.1 Hz. The system is excited for approximately 20 cycles at each frequency value, and the input and output acceleration data are collected using accelerometers with a sampling frequency of 1000 Hz. To illustrate the experimental data, we present the steady output acceleration of the system in the y- and z-directions. These responses are shown in Figs. 6 and 7, respectively. Note that the noise present in the output measured signals is removed by the use of a low-pass Butterworth filter in Matlab with a cutoff frequency of 50 Hz. We also use this filter to remove the noise from the FRFs. Fig. 8 shows a comparison between the unfiltered and filtered FRFs for a given excitation amplitude. We observe a good match between the unfiltered and filtered signals.

To identify the existence of nonlinearity in the system, we overlay the FRFs obtained from the sine-sweep tests in the y- direction with different excitation amplitudes. If the resonant frequencies in the FRF plot change with excitation amplitudes, it indicates the presence of nonlinearity.

From Fig. 9, we can observe that the system under analysis is nonlinear, as the resonant frequency (f_r) changes with the excitation amplitude in the y- direction. Nonlinear hysteresis is clearly observed, indicating that the system tracks different energy orbits in the forward and backward sweeps around resonance. In particular, the system shows higher maximum amplitude in the backward sweep at the same excitation level since it tracks the high energy orbits before the jump phenomena occurs. To identify the nature of nonlinearity, we plot the variation of f_r with the dynamic response (X_0), as shown in Fig. 10. The dynamic response of the system, i.e., X_0 represents the displacement of the prototype in y- (or z-) direction. It should be noted that the output X_0 is obtained by the numerical integration of the output acceleration data. From Fig. 10, we observe that f_r decreases as X_0 increases, indicating softening nonlinearity in the system.

To quantify this softening nonlinearity, we plot the variation of the equivalent stiffness K_{eq} ($= (2\pi f_r)^2\ m$) with X_0, and shown in Fig. 11. A quadratic function fits well for the experimental data in both forward and backward sweeps, given by Eqs. (10) and (11).

$$\text{Forward sweep} \quad K_{eqy} = 1.087 \times 10^6 - 5.724 \times 10^8 X_0 + 1.817 \times 10^{11} X_0^2, \tag{10}$$

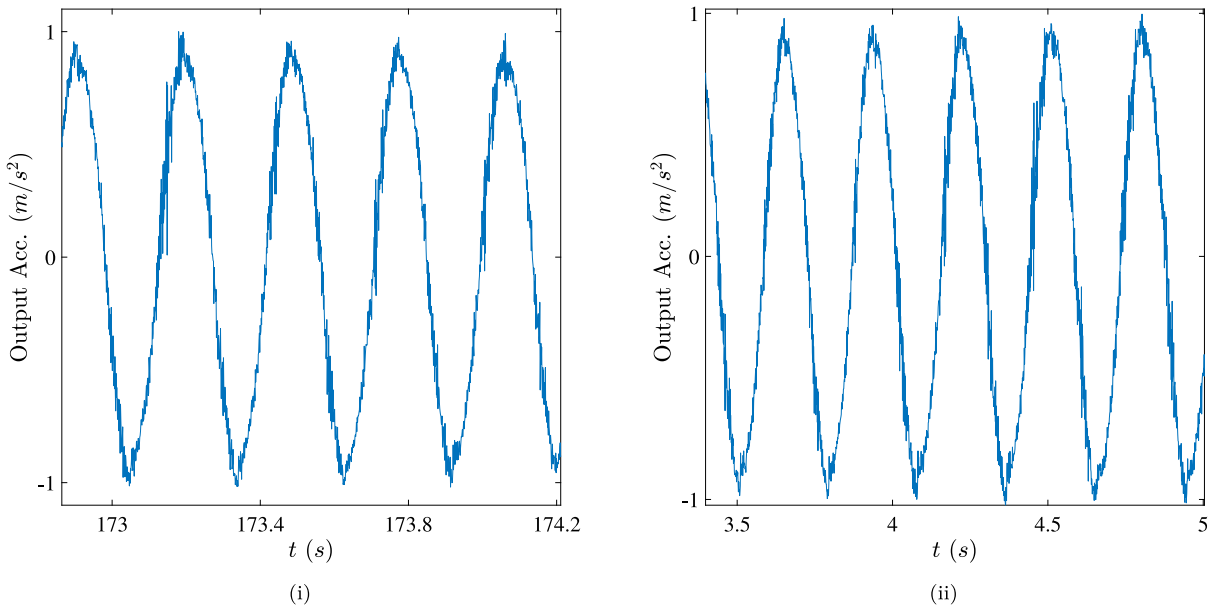

Fig. 7. Time response of the system in terms of output acceleration in z-direction for (i) in forward sweep, and (ii) in backward sweep.

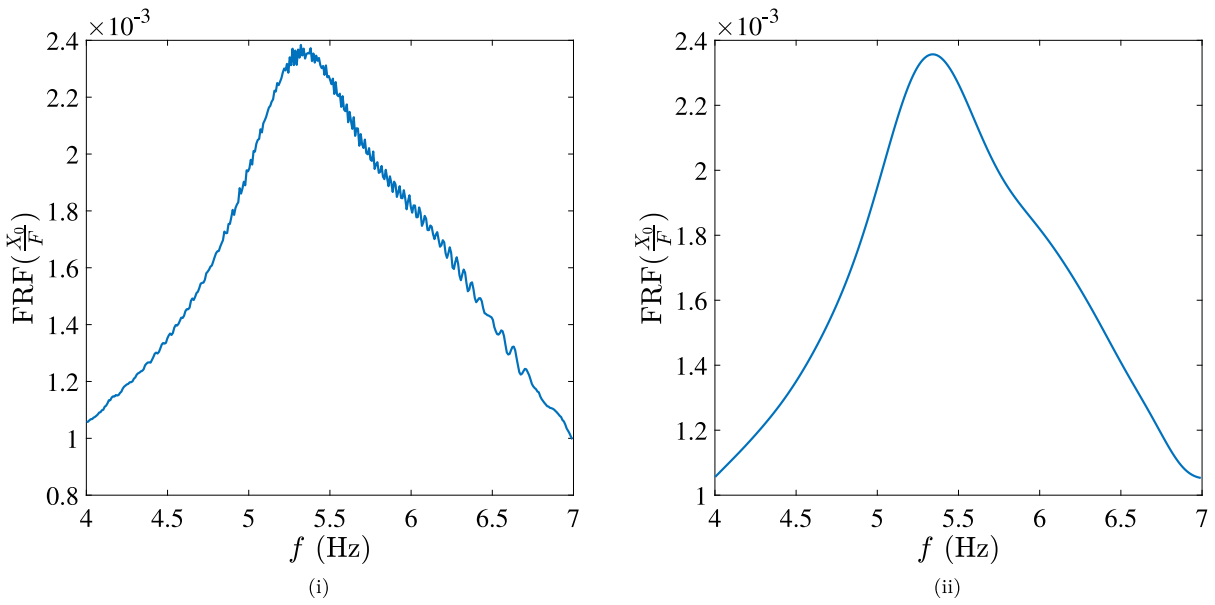

Fig. 8. (i) Unfiltered FRF (ii) filtered FRF of the dynamics response of the system in the y-direction during forward sweep.

$$\text{Backward sweep} \quad K_{eqy} = 1.074 \times 10^6 - 6.115 \times 10^8 X_0 + 1.958 \times 10^{11} X_0^2 . \tag{11}$$

Upon taking the average of the coefficients of different order in the polynomial corresponding to the forward and backward sweep (Eqs. (10)) and (11), we get

$$K^*_{eqy} = 1.0805 \times 10^6 - 5.9195 \times 10^8 X_0 + 1.8875 \times 10^{11} X_0^2 , \tag{12}$$

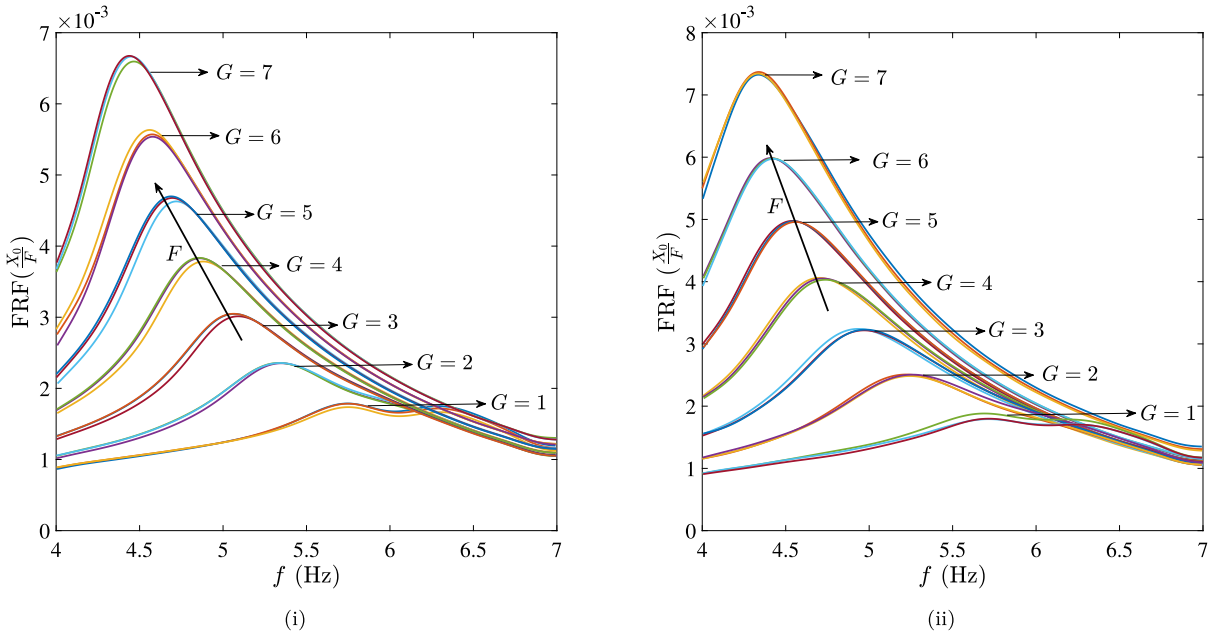

Fig. 9. Frequency response function of the prototype in the y-direction with increasing excitation amplitude for (i) forward sweep and (ii) backward sweep. G is the gain defined as normalized input voltage with respect to the minimum recorded input voltage which is used to drive the shaker.

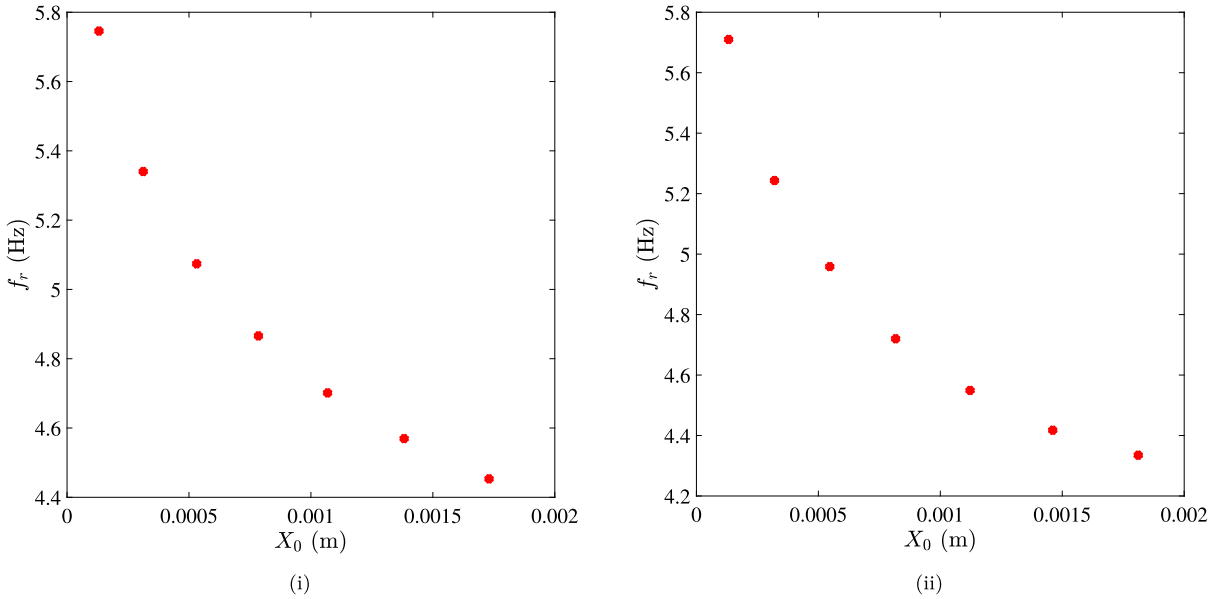

Fig. 10. Evolution of resonant frequency, f_r, in the y-direction with dynamic response X_0 for (i) forward sweep and (ii) backward sweep.

Accordingly, the nonlinear stiffness function can be obtained from the method of harmonic balance as (Eq. (7))

$$f_1(y) = 1.0805 \times 10^6 y(t) - 6.974 \times 10^8 |y(t)| y(t) + 2.51667 \times 10^{11} y(t)^3 . \tag{13}$$

Within the range of interest for vibration amplitude (i.e., the order of 1 mm), one can normalize Eq. (13) with respect to the vibration amplitude and linear stiffness (i.e., $\bar{y}(t) = y(t)/(1 \times 10^{-3})$ and $F_1(\bar{y}) = f_1(y)/(1 \times 10^{-3} \times 1.0805 \times 10^6)$) to get

$$F_1(\bar{y}) = \bar{y}(t) - 0.6454 |\bar{y}(t)| \bar{y}(t) + 0.2329 \bar{y}(t)^3 . \tag{14}$$

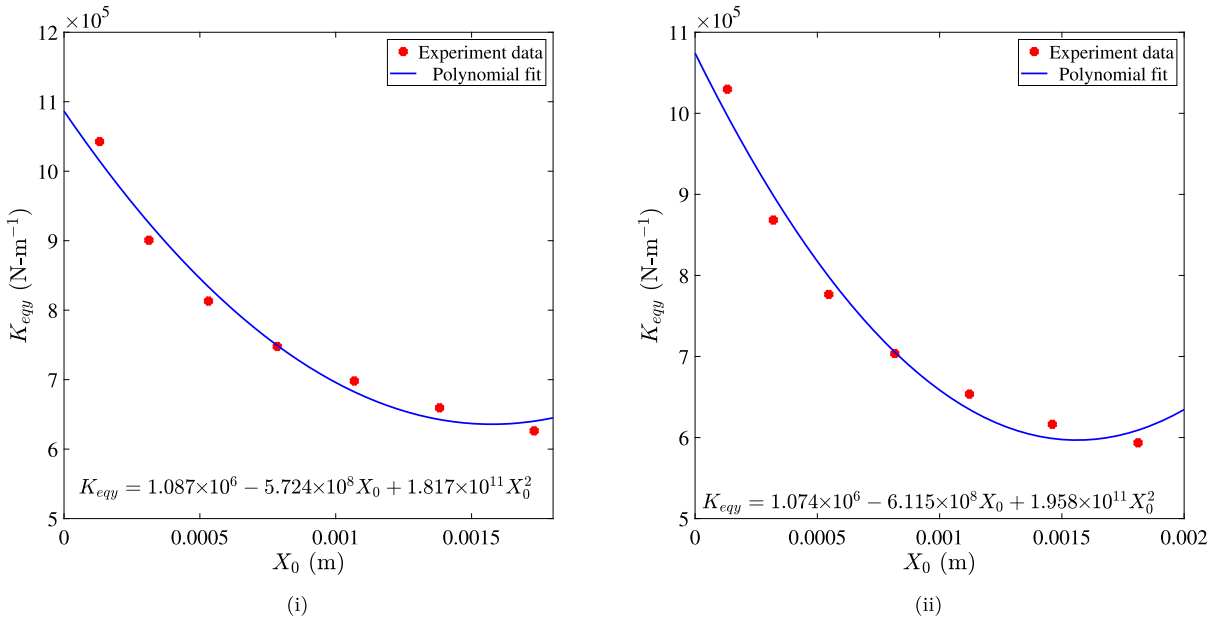

Fig. 11. Identification of nonlinear stiffness in the y-direction for (i) forward sweep and (ii) backward sweep.

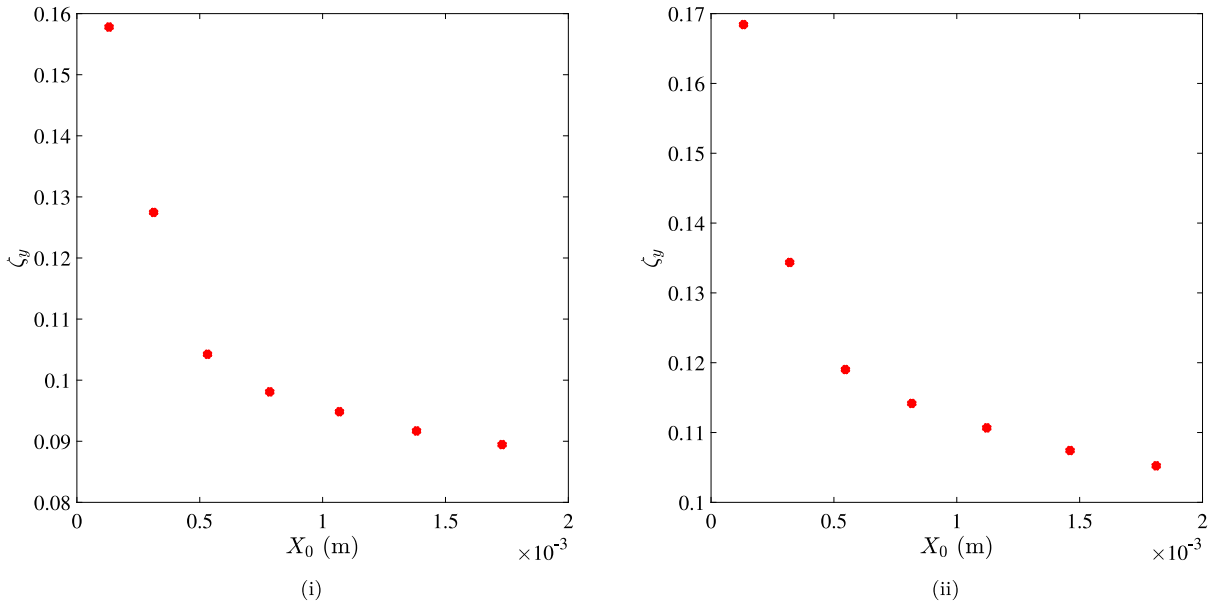

Fig. 12. Evolution of damping ratio (ζ_y) in the y-direction with dynamic response X_0 for (i) forward sweep and (ii) backward sweep.

From the above expression of nonlinear restoring force in the y-direction, it can be observed that the cubic term dominates the system dynamics for significantly higher perturbation values (high excitation amplitude) only. For moderately smaller displacement values, quadratic nonlinearity dominates the system dynamics.

To investigate the nonlinearity in the damping force in the y-direction, the damping ratio (ζ_y) is plotted against X_0 using the half-power bandwidth method. This variation is shown in Fig. 12. The plot in Fig. 12 shows that ζ_y decreases with increasing X_0, indicating softening nonlinearity in damping. Further, the variation of the equivalent damping coefficient C_{eqy} ($= 2\zeta_y\omega_r m$) with the amplitude of system velocity ($X_0\omega$) is shown in Fig. 13. We observe that the quadratic fitting function fits well with the obtained experimental data. These fitting functions for C_{eqy}, corresponding to forward and backward sweeps, are

$$\text{Forward sweep} \quad C_{eqy} = 1.009\times10^{4} - 3.212\times10^{5}(X_0\omega) + 4.166\times10^{6}(X_0\omega)^2\,, \tag{15}$$

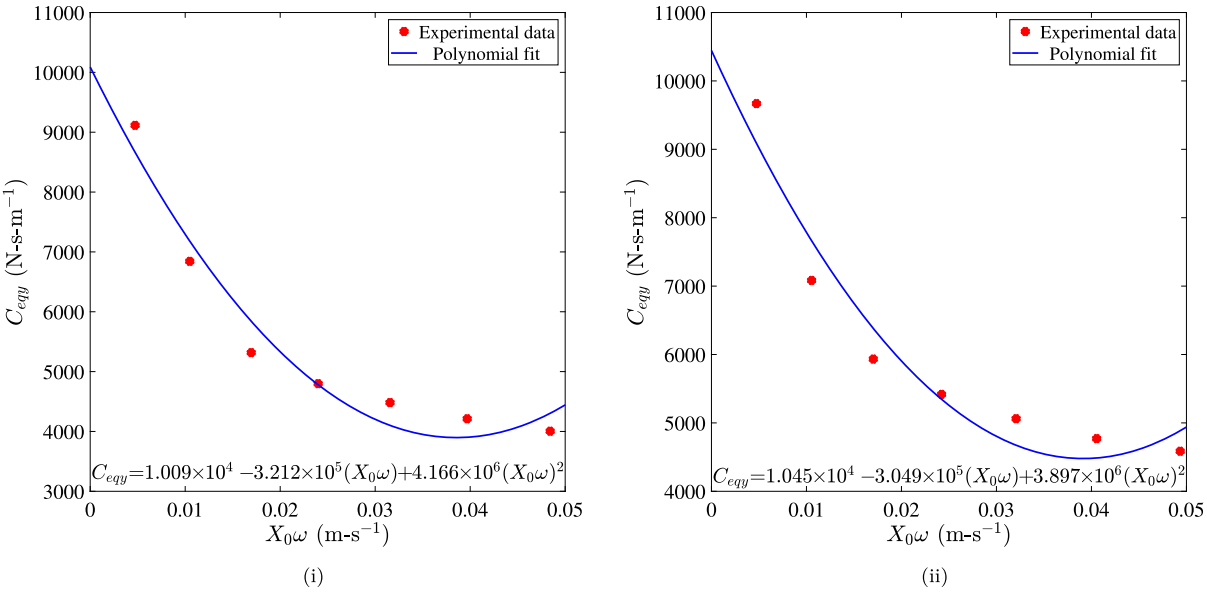

Fig. 13. Identification of nonlinear damping in the y-direction for (i) forward sweep and (ii) backward sweep.

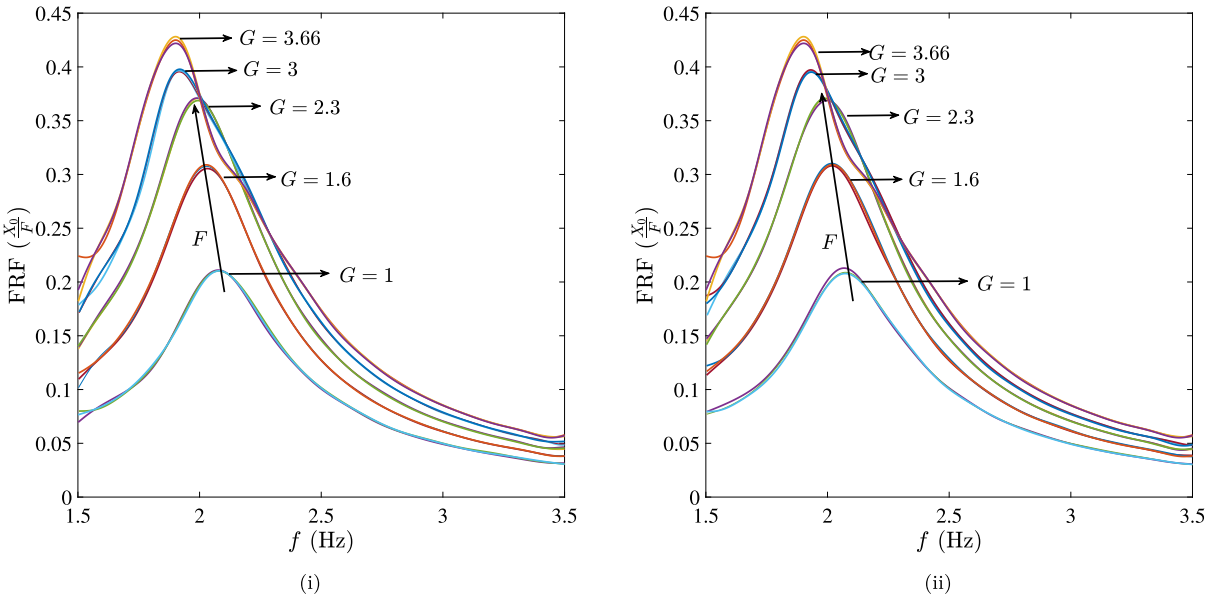

Fig. 14. Frequency response function of the prototype in the z-direction with increasing excitation amplitude for (i) forward sweep and (ii) backward sweep. G is the gain defined as normalized input voltage with respect to the minimum recorded input voltage which is used to drive the shaker.

$$\text{Backward sweep} \quad C_{eqy} = 1.045 \times 10^4 - 3.049 \times 10^5 (X_0\omega) + 3.897 \times 10^6 (X_0\omega)^2 . \tag{16}$$

Hence, upon taking the average of the different orders in Eqs. (15) and (16), the average equivalent damping coefficient given by

$$C^*_{eqy} = 1.027 \times 10^4 - 3.1305 \times 10^5 (X_0\omega) + 4.0315 \times 10^6 (X_0\omega)^2 . \tag{17}$$

Accordingly, the nonlinear damping function of the pneumatic isolator in the y-direction can be obtained through the method of harmonic balance as

$$g_1(\dot{y}) = 1.027 \times 10^4 \dot{y}(t) - 3.6880 \times 10^5 |\dot{y}(t)| \dot{y}(t) + 5.3753 \times 10^6 \dot{y}(t)^3 . \tag{18}$$

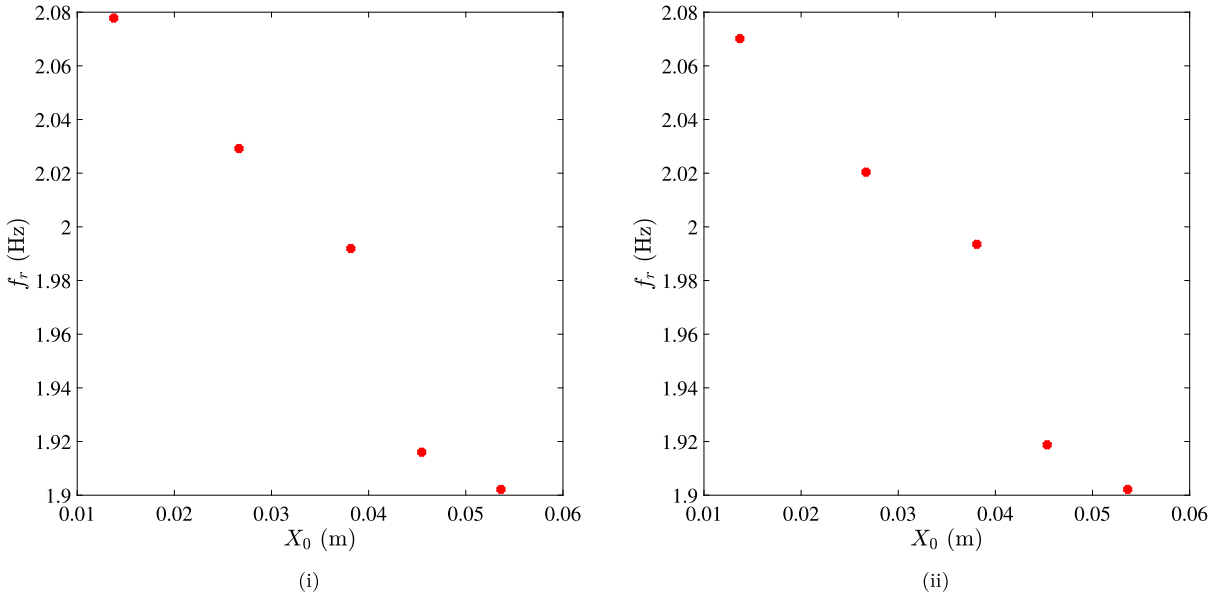

Fig. 15. Evolution of resonant frequency f_r in the z-direction with dynamic response X_0 for (i) forward sweep, and (ii) backward sweep.

Following the same procedure outlined above to obtain Eq. (14), one can normalize Eq. (18) within the range of interest (i.e., at the order of 10 mm/s) as

$$\bar{g}_1 = \dot{\bar{y}}(t) - 0.3591|\dot{\bar{y}}(t)|\dot{\bar{y}}(t) + 0.0523\dot{\bar{y}}(t)^3 . \tag{19}$$

From Eq (19), we can again conclude that quadratic nonlinearity dominates the system dynamics in case of moderate perturbations.

After establishing the nature of nonlinearity in the restoring force and damping force in the y-direction, we proceed to analyze the z-direction. Similar to the analysis in the y-direction, the frequency response functions (FRFs) corresponding to multiple excitation amplitudes in the z-direction are overlaid in Fig. 14. From Fig. 14, we can observe that the f_r corresponding to different FRFs changes with the excitation amplitude, indicating nonlinearity in the stiffness function of the pneumatic isolator in the z-direction. To further explore the nature of nonlinearity, we plot the variation of the f_r with X_0 in the z-direction as shown in Fig. 15. From Fig. 15, we observe that the f_r decreases with an increase in X_0, further confirming the existence of softening nonlinearity also in the z-direction. To quantify this softening nonlinearity, we plot the variation of the equivalent stiffness K_{eqz} with X_0 and fit the experimental data using a polynomial function as shown in Fig. 16. As shown in Fig. 16, the quadratic polynomial fits the experimental data well. These polynomial fits in the forward and backward sweeps are given by

$$\text{Forward sweep} \quad K_{eqz} = 1.424 \times 10^5 - 3.817 \times 10^5 X_0 - 3.016 \times 10^6 X_0^2 , \tag{20}$$

$$\text{Backward sweep} \quad K_{eqz} = 1.404 \times 10^5 - 3.189 \times 10^5 X_0 - 3.418 \times 10^7 X_0^2 . \tag{21}$$

Accordingly, the average K_{eqz} can be obtained by taking the average of the coefficients of quadratic fits in the forward and backward sweep (Eqs. (20) and (21)) and is given by

$$K^*_{eqz} = 1.414 \times 10^5 - 3.503 \times 10^5 X_0 - 3.217 \times 10^6 X_0^2 . \tag{22}$$

Thus, the nonlinear stiffness function of the pneumatic isolator in the z-direction can be obtained from the method of harmonic balance as

$$f_2(z) = 1.414 \times 10^5 z(t) - 4.126 \times 10^5 |z(t)|z(t) - 4.289 \times 10^6 z(t)^3 . \tag{23}$$

Further, within the range of interest for vibration amplitude (i.e., at the order of 10 mm), we normalize the above equation with respect to the vibration amplitude and linear stiffness (i.e., $\bar{z}(t) = z(t)/1 \times 10^{-2}$ and $F_2(\bar{z}) = f_2(z)/(1 \times 10^{-2} \times 1.414 \times 10^6)$) as

$$F_2(z) = \bar{z}(t) - 0.0292|\bar{z}(t)|\bar{z}(t) + 0.003\bar{z}(t)^3 . \tag{24}$$

From Eq. (24), it can be noted that for moderately small amplitudes, quadratic nonlinearity in the restoring force dominates system dynamics in the z-direction also.

To investigate the existence of nonlinearity in damping in the z-direction, we plot the damping ratio ζ_z against X_0 as shown in Fig. 17. From Fig. 17, it can be observed that the damping ratio decreases with increasing X_0, indicating softening nonlinearity in damping. Furthermore, the variation of the equivalent damping coefficient in the z-direction, C_{eqz}, with velocity amplitude $X_0\omega$ is

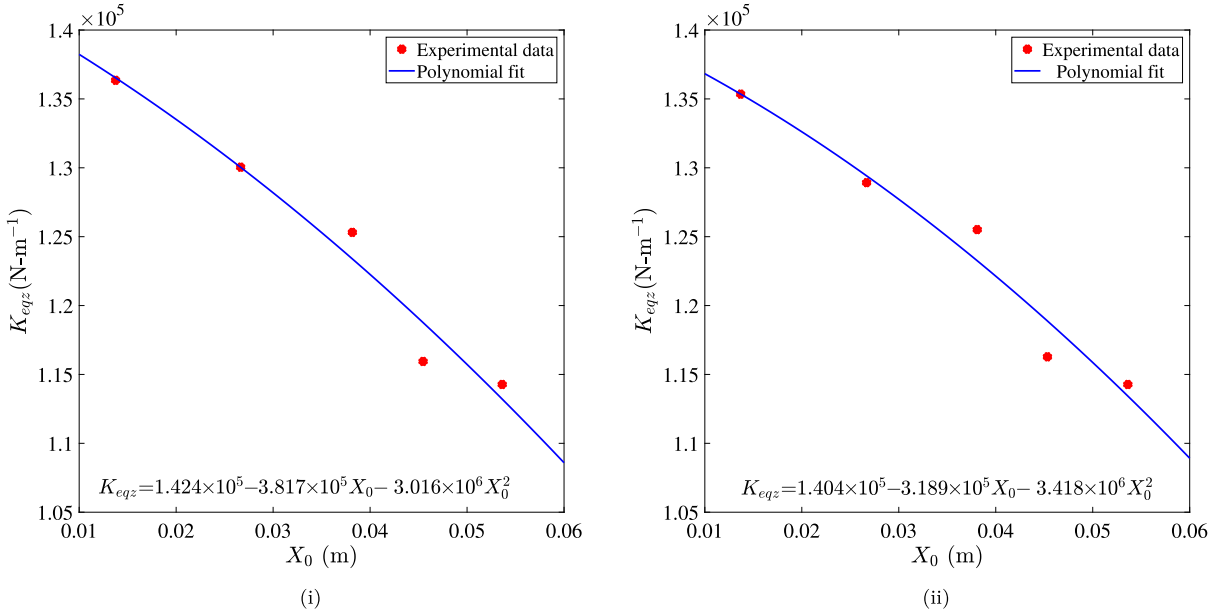

Fig. 16. Identification of nonlinear stiffness in the z-direction for (i) forward sweep and (ii) backward sweep.

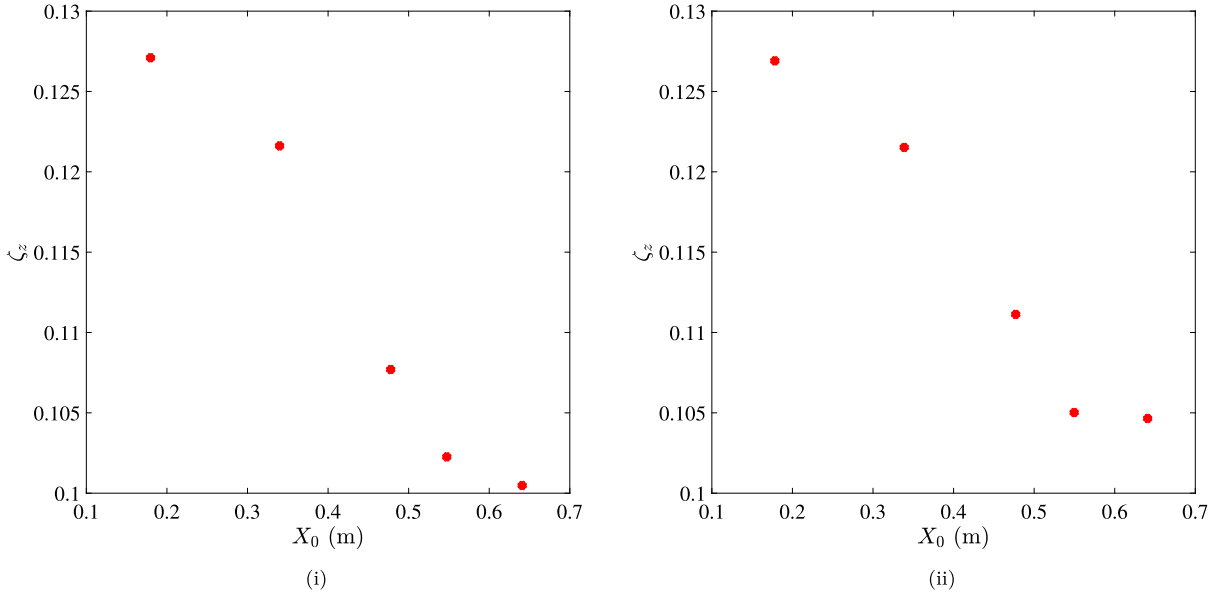

Fig. 17. Evolution of damping ratio (ζ_z) in the z-direction with dynamic response X_0 for (i) forward sweep and (ii) backward sweep.

shown in Fig. 18. We observe that a quadratic fit describes this variation well; the equations for the forward and backward sweeps are

$$\text{Forward sweep} \quad C_{eqz} = 2656 - 1252(X_0\omega) + 526.1(X_0\omega)^2\,, \tag{25}$$

$$\text{Backward sweep} \quad C_{eqz} = 2620 - 1114(X_0\omega) + 592.2(X_0\omega)^2\,. \tag{26}$$

The average equivalent damping coefficient and accordingly, the nonlinear damping function of the pneumatic isolator in the z-direction are

$$\text{Average} \quad C^*_{eqz} = 2638 - 1183(X_0\omega) + 559.15(X_0\omega)^2\,, \tag{27}$$

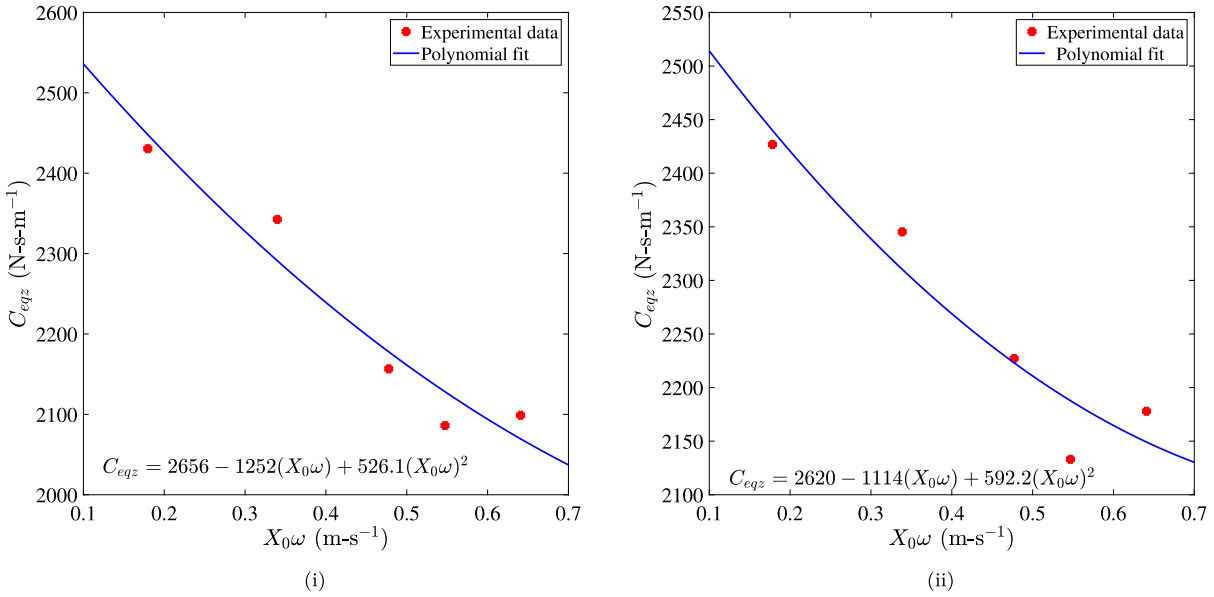

Fig. 18. Identification of nonlinear damping in the z-direction for (i) forward sweep, and (ii) backward sweep.

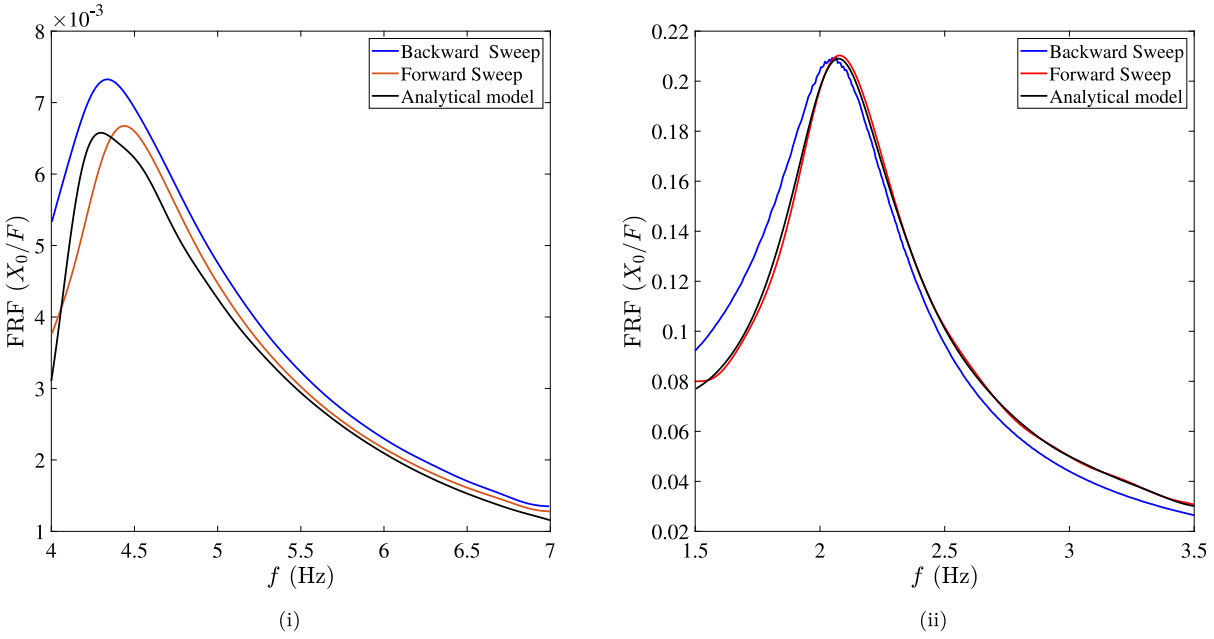

Fig. 19. Comparison of experimental results with empirical model in the (i) y-direction, and (ii) z-direction.

$$\text{Damping function} \quad g_2(\dot{z}) = 2638\dot{z}(t) - 1393|\dot{z}(t)|\dot{z}(t) + 745.533\dot{z}(t)^3 \,. \tag{28}$$

Following the same procedure applied to obtain Eq. (14), one can normalize the above damping function within the range of interest (i.e., at the order of 100 mm/s) as

$$\bar{g}_2 = \dot{\bar{z}}(t) - 0.0528|\dot{\bar{z}}(t)|\dot{\bar{z}}(t) + 0.0028\dot{\bar{z}}(t)^3 \tag{29}$$

Based on the derived models for the stiffness and damping characteristics of the pneumatic isolator (Eqs. (13), (18), (23), (28)), we observe that within the investigated range of dynamic response, the quadratic softening characteristics of the pneumatic isolator dominate the system dynamics in both y and z-directions. However, for dynamic responses beyond the range considered in this

study, higher-order nonlinear terms (e.g., cubic, quartic) should be included in the curve-fitting to improve the accuracy of the predicted pneumatic isolator's stiffness and damping characteristics. The measured response and the empirical models are compared in Fig. 19(i) and (ii) for the y and z-directions, respectively. It is apparent from Fig. 19(i) and (ii) that the identified models exhibit softening behavior in both directions. Moreover, the identified models demonstrate a reasonably good ability to predict the system's behavior within the investigated range. With the nonlinear characteristics of the system established, we proceed to present the linear stability analysis of the system, considering a wider range of excitation forces and frequencies, in the subsequent section.

5. Linear stability analysis

In this section, we present the linear stability analysis of the system with nonlinear stiffness and damping characteristics as identified in Section 4. We start with the linear stability analysis in the y-direction. Since the motions of the prototype in the y- and z-directions are uncoupled for the current analysis, the governing equation of motion in the y-direction is

$$\begin{aligned} &m\ddot{y} + 1.027\times10^{4}\dot{y} - 3.6880\times10^{5}|\dot{y}|\dot{y} + 5.3753\times10^{6}\dot{y}^{3} + 1.0805\times10^{6}y(t) - 6.974\times10^{8}|y(t)|y(t) \\ &+ 2.51667\times10^{11}y(t)^{3} = F_{0}\sin(2\pi f t)\,. \end{aligned} \tag{30}$$

In the above equation, F_0 represents the excitation amplitude, and f is the excitation frequency. Since Eq. (30) is a nonautonomous system with a harmonic excitation, the steady-state will always be periodic instead of constant as in the case of an autonomous system. Additionally, Eq. (30) is a non-smooth, nonlinear differential equation due to the presence of $|y|$ and $|\dot{y}|$; therefore, we use a numerical fixed arc-length continuation scheme to obtain the steady-state periodic solutions for different values of f and for a given value of F_0. If y_s is the steady-state solution of the system in the y-direction for the given value of excitation amplitude and frequency, then the perturbed solution of Eq. (30) can be written as

$$y(t) = y_s(t) + \epsilon\eta(t)\,, \tag{31}$$

where $\eta(t)$ is an $\mathcal{O}(1)$ quantity and ϵ is a small parameter ($\ll 1$). Since the steady-state periodic solutions, i.e., y_s, of Eq. (31) satisfy Eq. (30), we get the linearized equations in terms of perturbation and the steady-state as

$$\begin{aligned} &m\ddot{\eta} + 1.027\times10^{4}\dot{\eta} - 7.3760\times10^{5}|\dot{y}_s|\dot{\eta} + 16.1259\times10^{6}\dot{y}_s^{2}\dot{\eta} + 1.0805\times10^{6}\eta - 13.9480\times10^{8}|y_s|\eta \\ &+ 7.55\times10^{11}y_s^{2}\eta = 0\,. \end{aligned} \tag{32}$$

Note that Eq. (32) involves time-periodic coefficients in terms of the steady states; therefore, we use the Floquet theory to determine the stability of the steady-state periodic solutions numerically in the parametric space of F_0 and f. To get the stability in the space of $F_0 - f$, we divide the given range of F_0 and f in 1000×500 sub-regions with 1000 discrete points along the F_0-axis and 500 discrete points along the f-axis. We emphasize that we have chosen the frequency range from 4–8 Hz for the stability analysis, i.e., around the system's natural frequency in the y-direction. In the next step, we run numerical simulations to generate the fundamental matrix and obtain the Floquet multipliers as the eigenvalues of the fundamental matrix. If the magnitude of the dominant Floquet multiplier at a grid point is less than one, the system is stable at that point; if it is greater than one, the system becomes unstable. Therefore, the stability boundary is defined as the locus of operating points corresponding to the dominant Floquet multiplier with magnitude one. Upon conducting the stability analysis, we did not observe any linearly unstable regimes for the considered range of excitation and amplitude, and hence, the considered parametric space is always stable.

Next, we present the linear stability analysis of the system in the z-direction. With the identified nonlinear stiffness and damping characteristics, the governing equation of motion in the z-direction is given by

$$\begin{aligned} &m\ddot{z} + 2638\dot{z} - 1393|\dot{z}|\dot{z} + 745.533\dot{z}^{3} + 1.414\times10^{5}z(t) - 4.126\times10^{5}|z|z \\ &- 4.289\times10^{6}z^{3} = F_{0}\sin(2\pi f t)\,. \end{aligned} \tag{33}$$

Similar to the analysis in the y-direction, we find the steady-state periodic solutions of the system in the z-direction numerically via the fixed arc-length continuation scheme. Therefore, if $z_s(t)$ represents the steady-state periodic solution, then the perturbed solution of Eq. (33) can be written as

$$z(t) = z_s(t) + \epsilon\phi(t)\,. \tag{34}$$

where $\phi(t)$ is an $\mathcal{O}(1)$ quantity and ϵ is a small parameter ($\ll 1$). Substitution of Eq. (34) in Eq. (33) leads to the linearized equation as

$$\begin{aligned} &m\ddot{\phi} + 2638\dot{\phi} - 2786|\dot{z}_s|\dot{\phi} + 2.2366\times10^{3}\dot{z_s}^{2}\dot{\phi} + 1.414\times10^{5}\phi - 8.2520\times10^{5}|z_s|\phi \\ &- 12.8670\times10^{6}z_s^{2}\phi = 0\,. \end{aligned} \tag{35}$$

Again, we utilize the Floquet theory to determine the system's stability in the z-direction. We repeat the procedure as outlined above for stability in the y-direction. However, for the stability analysis in the z direction, we select the frequency range from 1 to 4 Hz, which is around the system's natural frequency in the z-direction. Similar to the observation drawn for the y-direction, we observe that the UPM prototype with pneumatic isolator remains stable in z-direction for the given range of excitation amplitude and frequency.

To further verify these observations, we perturb the steady-state periodic solution at higher excitation amplitude and around the resonant frequency to observe its evolution with time in y and z-directions. These motions in y- and z-directions are shown in

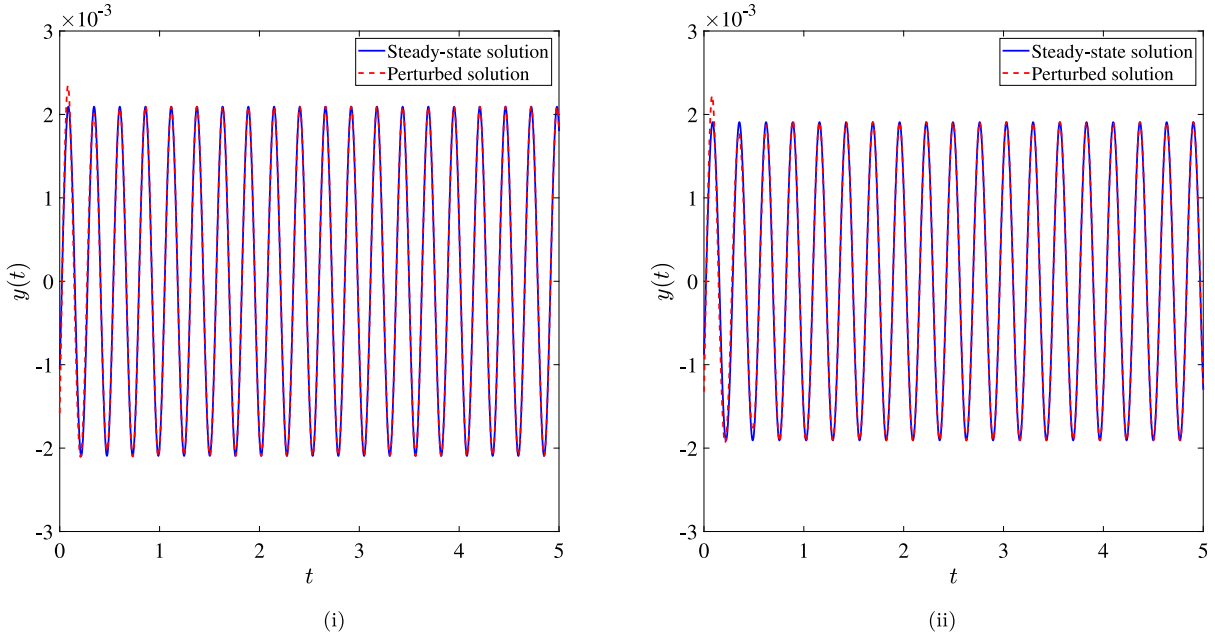

Fig. 20. Comparison of steady-state time-response with the time response for perturbed initial conditions in the y-direction (i) $F_0 = 419.8$ N, $f = 3.8831$ Hz, and (ii) $F_0 = 459.9$ N, $f = 3.739$ Hz.

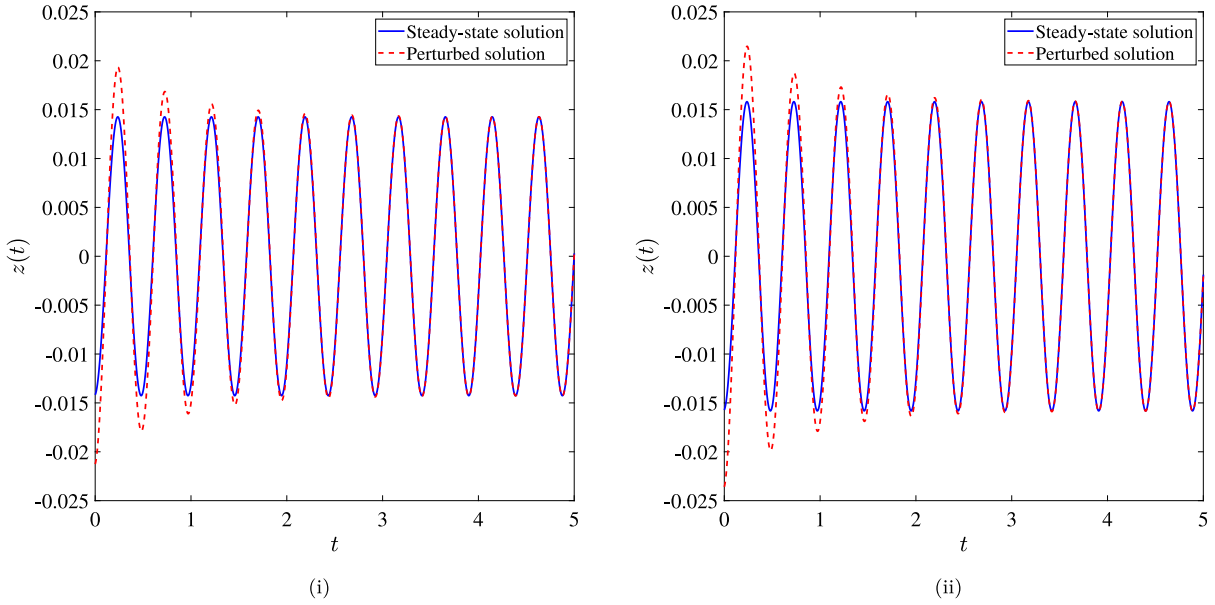

Fig. 21. Comparison of steady-state time-response with the time response for perturbed initial conditions in the z-direction for (i) $F_0 = 450.5$ N, $f = 2.0470$ Hz, and (ii) $F_0 = 494.5892$ N, $f = 2.0426$ Hz.

Figs. 20 and 21, respectively. Both figures show that any initial perturbation dies out with time and the system settles down to a steady-state periodic solution. This observation verifies our linear stability analysis in the y- and z-direction.

It should be noted here that these identified nonlinear parameters are the functions of the pressure inside the pneumatic chamber. Hence, we can have different sets of nonlinear parameters (with similar nonlinear behavior) for different pressure values that will increase the system's instability.

To explore the system dynamics for different possible stiffness and damping functions of the pneumatic isolator, we perform the bifurcation analysis of the system's response in y-direction with a modified damping function. For this, we assume that the damping

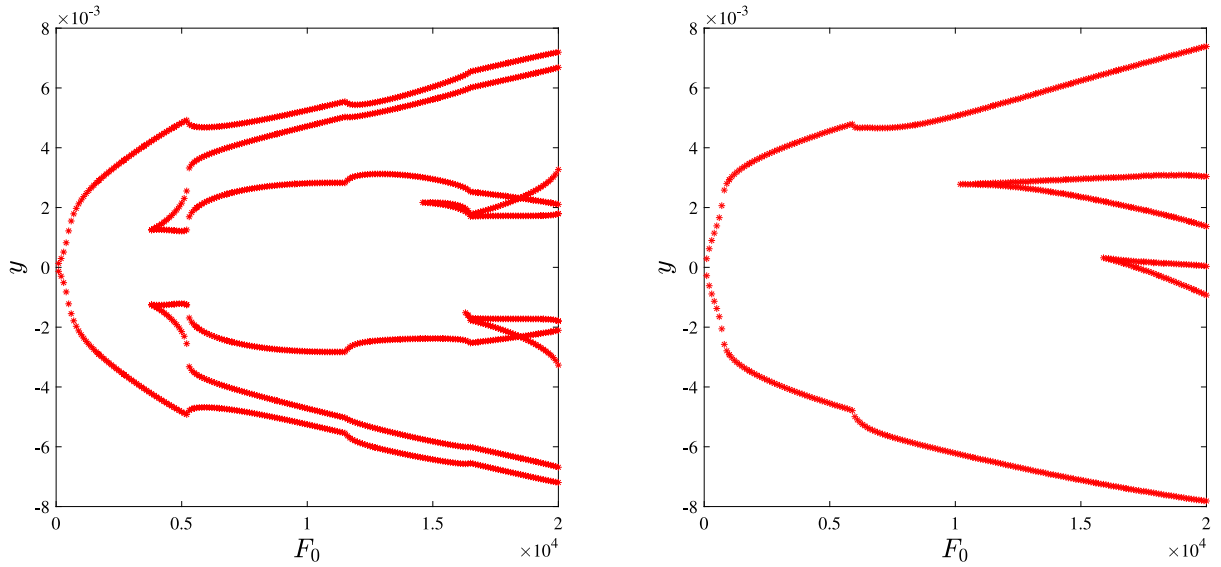

Fig. 22. Numerical bifurcation diagram for the response of the system in y-direction with varying values of excitation amplitude for (i) $f = 3$ Hz, and (ii) $f = 5$ Hz.

characteristics of the pneumatic isolator in the transverse direction is primarily governed by quadratic nonlinearity as

$$g_1(\dot{y}) = 1.027 \times 10^4 \dot{y}(t) - 3.6880 \times 10^3 |\dot{y}(t)| \dot{y}(t)\,. \tag{36}$$

while we use the same stiffness function in the y-direction (Eq. (13)). In the next step, we evolve the system dynamics with time for different excitation amplitude values and at a given excitation frequency. We use Matlab built-in command 'ode45' to evolve system dynamics with high absolute and relative tolerance values ($1e^{-10}$). The numerical bifurcation diagram of the system's response in y-direction is shown in Fig. 22 for two different values of excitation frequencies, in particular, low frequency ($f = 3$ Hz) and around resonant frequency ($f = 5$ Hz) in Fig. 22(i) and (ii), respectively. From Fig. 22(i), we can observe that the system's stable periodic response remains stable for moderately high values of excitation amplitude, viz. $F_0 < 3800$. However, any further increase in the value of F_0 causes the system's stable periodic response to become unstable and transition to period-2 and period-4 solutions. The bifurcation of the stable periodic solution to period-2 solution through period-doubling bifurcation can also be seen through phase portrait and is shown in Fig. 23. Furthermore, Fig. 22(ii) shows the numerical bifurcation diagram of the system in the y- direction for $f = 5$ Hz. From Fig. 22(ii), we can observe that similar to the $f = 3$ Hz system's stable periodic response becomes unstable, and the system exhibits period-2 solutions. However, unlike the case of $f = 3$ Hz, the bifurcation point shifts toward the right, i.e., for higher excitation amplitude. This loss of stability of stable-periodic solutions for $f = 5$ Hz has been shown through phase portraits in Fig. Fig. 24.

To this end, we emphasize that in the current analysis, the effect of mode coupling between y and $z-$ directions has not been considered. The nonlinear mode coupling in the system can give rise to more complex dynamical solutions and is left for future work.

6. Conclusion

In this study, we identified the nonlinearities in stiffness and damping characteristics of a pneumatic isolator, qualitatively and quantitatively. For this purpose, we used experimental data and equivalent analytical approaches (the harmonic balance method and the half-power bandwidth method). The pneumatic isolators were modeled as spring-damper systems in the y and z-directions, and the equivalent stiffness and damping characteristics were determined by analyzing the frequency response function curves. The frequency response curves at different excitation levels were utilized to identify the variation of resonant frequency and hence, equivalent stiffness with the dynamic response. The relationship between equivalent stiffness and dynamic response was identified through thepolynomial curve-fitting approach. Additionally, the half-power bandwidth method was employed to determine the damping ratio and subsequently the damping coefficients in both the y- and z-directions. Once equivalent stiffness and damping coefficients were known, the nonlinear stiffness function and damping functions were obtained through the method of harmonic balance. Our findings revealed the presence of softening nonlinearity in both the stiffness and damping characteristics of the pneumatic isolator in the y- and z-directions. Furthermore, this softening nonlinearity was modeled through a combination of cubic stiffness and cubic damping functions in the y- and z-directions. It is worth noting that although cubic nonlinearity was

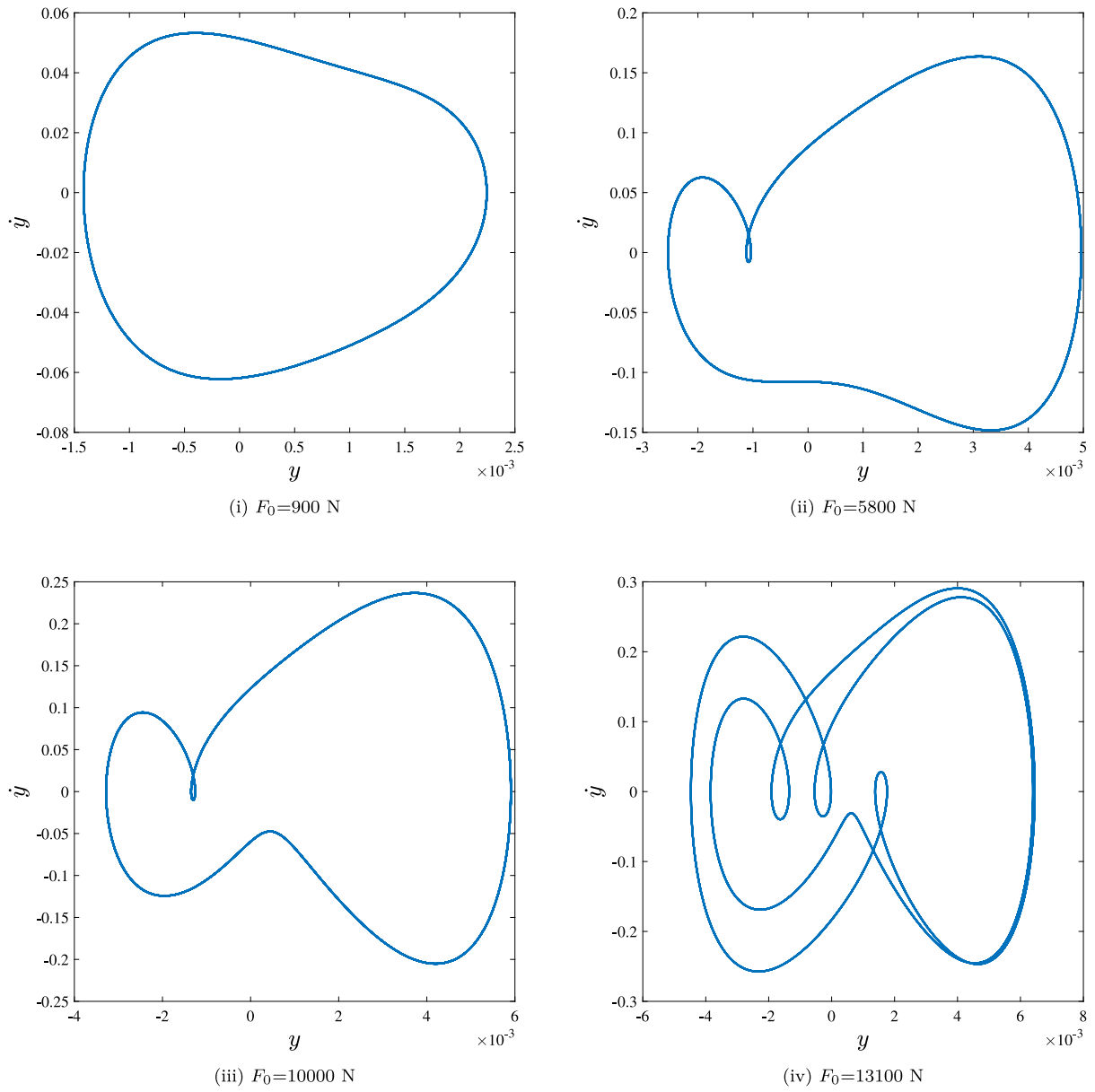

Fig. 23. Phase portraits for the response of the system in y-direction for different values of excitation amplitude and $f = 3$ Hz.

present in the system, quadratic nonlinearity was found to dominate the system dynamics for moderately small amplitude vibrations. Furthermore, the linear stability analysis of the system was carried out to explore the stability of the steady-state periodic solutions in the regime of excitation amplitude and frequency for the identified nonlinear parameters. We observed that the steady-state periodic solutions remain stable for a given range of excitation amplitude and frequency for the identified stiffness and damping parameters. Furthermore, we observed a slight change in the damping characteristics could introduce instability in the system in the form of period-2 and period-4 solutions.

Finally, the original contributions of this paper can be summarized as (1) identification of nonlinearity in stiffness and damping characteristics of a pneumatic isolator, (2) quantification of these nonlinearities in stiffness and damping as functions of displacement and velocity, (3) exploration of instability in the parametric space of excitation amplitude and frequency with the identified

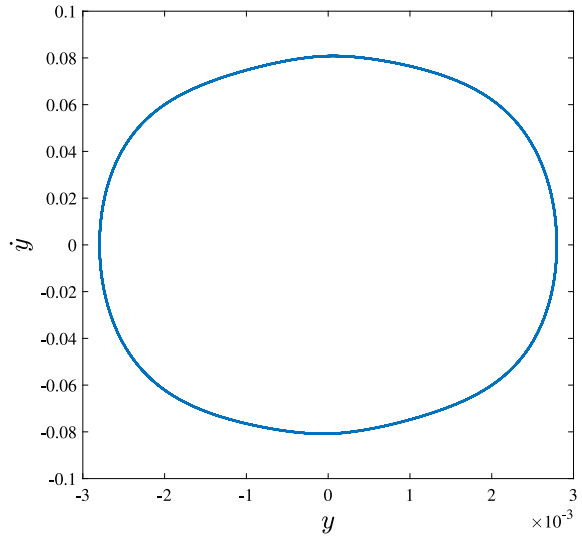

(i) F_0=900 N

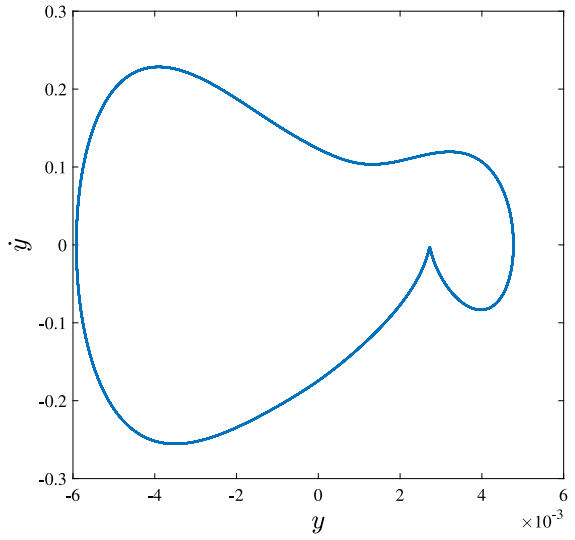

(ii) F_0=5800 N

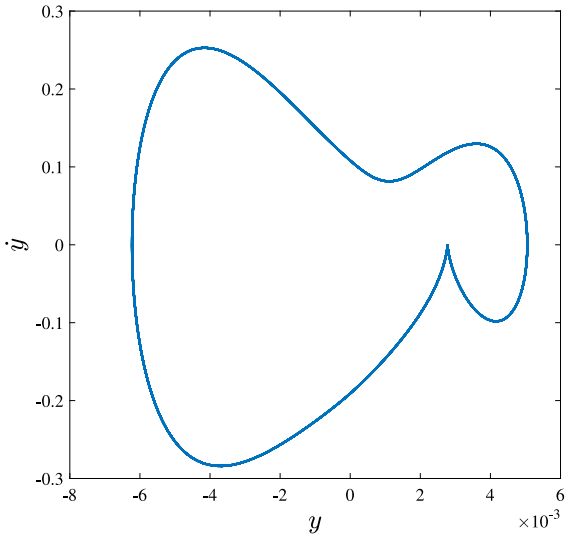

(iii) F_0=10000 N

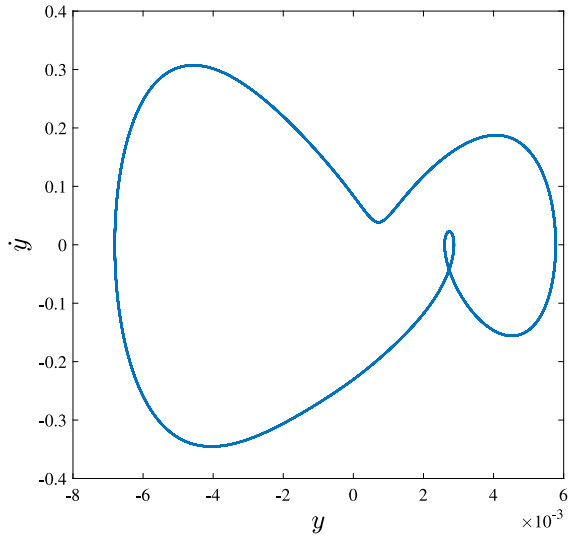

(iv) F_0=13100 N

Fig. 24. Phase portraits for the response of the system in y-direction for different values of excitation amplitude and $f = 5$ Hz.

parameters, and (4) exploration of complex motions of the system for a given value of frequency and different values of excitation amplitudes.

Declaration of competing interest

The authors declare that they have no conflict of interest.

Data availability

Data will be made available on request.

Acknowledgments

This work is funded by National Science Foundation (NSF), United States CMMI #2000984: Nonlinear Dynamics of Pneumatic Isolators in Ultra-Precision Manufacturing Machines.

References

[1] C.G. Gordon, Generic vibration criteria for vibration-sensitive equipment, in: Optomechanical Engineering and Vibration Control, vol. 3786, International Society for Optics and Photonics, SPIE, 1999, pp. 22–33, http://dx.doi.org/10.1117/12.363802.
[2] J. Lee, C.E. Okwudire, Reduction of vibrations of passively-isolated ultra-precision manufacturing machines using mode coupling, Precis. Eng. 43 (2016) 164–177.
[3] C.E. Okwudire, J. Lee, Minimization of the residual vibrations of ultra-precision manufacturing machines via optimal placement of vibration isolators, Precis. Eng. 37 (2013) 425–432.
[4] T. Masuzawa, State of the art of micromachining, CIRP Ann. 49 (1) (2000) 473–488.
[5] L. Alting, F. Kimura, H.N. Hansen, G. Bissacco, Micro engineering, CIRP Ann. 52 (2) (2003) 635–657.
[6] H.N. Hansen, K. Carneiro, H. Haitjema, L. Chiffre, Dimensional micro and nano metrology, CIRP Ann. 55 (2) (2006) 721–743.
[7] K.F. Ehmann, A synopsis of US micro-manufacturing research and development activities and trends, Borovets, Bulgaria, 2007, pp. 7–13.
[8] D. DeBra, Vibration isolation of precision machine tools and instruments, CIRP Ann. 41 (1992) 711–718.
[9] P.K. Subrahmanyan, D. Trumper, Synthesis of passive vibration isolation mounts for machine tools - a control systems paradigm, in: Proceedings of the 2000 American Control Conference. ACC (IEEE Cat. No.00CH36334), vol. 4, 2000, pp. 2886–2891 vol.4.
[10] P.P. Schellekens, N. Rosielle, H. Vermeulen, M.M. Vermeulen, S.S. Wetzels, W. Pril, Design for precision : current status and trends, CIRP Ann. 47 (1998) 557–586.
[11] D. Karnopp, Active and semi-active vibration isolation, J. Mech. Des. 117 (1995) 177–185.
[12] Y. Liu, T.P. Waters, M. Brennan, A comparison of semi-active damping control strategies for vibration isolation of harmonic disturbances, J. Sound Vib. 280 (2005) 21–39.
[13] E. Rivin, Vibration isolation of precision objects, Sound Vib. 40 (2006) 12–20.
[14] C. Erin, B. Wilson, J. Zapfe, An improved model of a pneumatic vibration isolator : Theory and experiment, J. Sound Vib. 218 (1998) 81–101.
[15] Y. Shin, K. Kim, P.H. Chang, D.K. Han, Three degrees of freedom active control of pneumatic vibration isolation table by pneumatic and time delay control technique, J. Vib. Acoust. 132 (2010) 051013.
[16] J.I. Soliman, D. Tajer-Ardabili, Self-damped pneumatic isolator for variable frequency excitation, J. Mech. Eng. Sci. 8 (3) (1966) 284–293.
[17] P.C. Chen, M. Shih, Modeling and robust active control of a pneumatic vibration isolator, J. Vib. Control 13 (2007) 1553–1571.
[18] Y. Shin, K. Kim, Performance enhancement of pneumatic vibration isolation tables in low frequency range by time delay control, J. Sound Vib. 321 (2009) 537–553.
[19] V.M. Ryaboy, Static and dynamic stability of pneumatic vibration isolators and systems of isolators, J. Sound Vib. 333 (2014) 31–51.
[20] M. Bukhari, O. Barry, On the nonlinear vibration analysis of ultra precision manufacturing machines with mode coupling, in: ASME 2017 International Design Engineering Technical Conferences and Computers and Information in Engineering Conference, American Society of Mechanical Engineers Digital Collection, 2017.
[21] Z. Sihong, W. Jiasheng, Z. Ying, Research on theoretical calculation model for dynamic stiffness of air spring with auxiliary chamber, in: 2008 IEEE Vehicle Power and Propulsion Conference, IEEE, 2008, pp. 1–6.
[22] A.J. Nieto, A.L. Morales, A. Gonzalez, J.M. Chicharro, P. Pintado, An analytical model of pneumatic suspensions based on an experimental characterization, J. Sound Vib. 313 (1–2) (2008) 290–307.
[23] H. Pu, X. Luo, X. Chen, Modeling and analysis of dual-chamber pneumatic spring with adjustable damping for precision vibration isolation, J. Sound Vib. 330 (15) (2011) 3578–3590.
[24] T. Asami, Y. Yokota, T. Ise, I. Honda, H. Sakamoto, An approximate formula to calculate the restoring and damping forces of an air spring with a small pipe, J. Vib. Acoust. 135 (5) (2013).
[25] J.H. Lee, K. Kim, Modeling of nonlinear complex stiffness of dual-chamber pneumatic spring for precision vibration isolations, J. Sound Vib. 301 (2007) 909–926.
[26] M.F. Heertjes, N.V.D. Wouw, Nonlinear dynamics and control of a pneumatic vibration isolator, J. Vib. Acoust. 128 (2006) 439–448.
[27] D. Alejo, L. Isidro, R. Jesús, A. Alvarez, Parameter estimation of linear and nonlinear systems based on orthogonal series, Procedia Eng. 35 (2012) 67–76.
[28] S.M. Sajed Sadati, A.S. Nobari, T. Naraghi, Identification of a nonlinear joint in an elastic structure using optimum equivalent linear frequency response function, Acta Mech. 223 (7) (2012) 1507–1516.
[29] J.-P. Noël, G. Kerschen, E. Foltête, S. Cogan, Grey-box identification of a non-linear solar array structure using cubic splines, Int. J. Non-Linear Mech. 67 (2014) 106–119.
[30] X. Liu, L. Wang, Q. Chen, B. Sun, Parameter identification of structural nonlinearity by using response surface plotting technique, J. Shanghai Jiaotong Univ. (Science) (2020) 1–10.
[31] J. Prawin, A. Rama Mohan Rao, K. Lakshmi, Nonlinear identification of structures using ambient vibration data, Comput. Struct. 154 (2015) 116–134.
[32] M. Feldman, S. Braun, Nonlinear vibrating system identification via Hilbert decomposition, Mech. Syst. Signal Process. 84 (2017) 65–96.
[33] H. Jalali, H. Ahmadian, J.E. Mottershead, Identification of nonlinear bolted lap-joint parameters by force-state mapping, Int. J. Solids Struct. 44 (25–26) (2007) 8087–8105.
[34] S.J. Julier, J.K. Uhlmann, New extension of the Kalman filter to nonlinear systems, in: Signal Processing, Sensor Fusion, and Target Recognition VI, vol. 3068, Spie, 1997, pp. 182–193.
[35] S.K. Gupta, M.A. Bukhari, O.R. Barry, Nonlinear mode coupling in a passively isolated mechanical system, Nonlinear Dynam. 101 (4) (2020) 2055–2086.
[36] I. Wang, An analysis of higher order effects in the half power method for calculating damping, J. Appl. Mech. 78 (1) (2011).
[37] G.A. Papagiannopoulos, G.D. Hatzigeorgiou, On the use of the half-power bandwidth method to estimate damping in building structures, Soil Dyn. Earthq. Eng. 31 (7) (2011) 1075–1079.
[38] A.K. Zrayka, E. Mucchi, A comparison among modal parameter extraction methods, SN Appl. Sci. 1 (2019) 1–11.